ADVANCED QUANTUM TECHNOLOGIES
www.advquantumtech.com

Coherently Manipulated 2D Ion Crystal in a Monolithic Paul Trap

Ye Wang, Mu Qiao, Zhengyang Cai, Kuan Zhang, Naijun Jin, Pengfei Wang, Wentao Chen, Chunyang Luan, Botao Du, Haiyan Wang, Yipu Song, Dahyun Yum, and Kihwan Kim**

Using a 2D ion crystal for quantum simulation and computation has been pursued for a long time. The coherent manipulation of a stationary 2D crystal in the Paul trap may be hampered by the micromotion synchronous with the oscillating electric field. Here, a simple Paul trap that stably confines over 20 $^{171}Yb^{+}$ ions in a stationary 2D crystal is presented. The disturbance of the micromotion in coherent operations is mitigated by making the direction of micromotion perpendicular to the transverse direction of the 2D crystal. To achieve the condition of perpendicularity, the structure of the trap electrodes is comprehensively designed, which also provides the controllability of rotating principal axes. The transverse vibrational modes by Raman laser-beams are addressed and coherent evolution of sideband transitions on these modes observed. Moreover, this trap allows for optical access with a 0.86 numerical aperture which facilitates applying individually addressing laser-beams. This work can be an example of realizing a 2D-trapped-ion based quantum simulator and computer in a Paul trap.

1. Introduction

The 2D ion crystal can be an attractive and natural platform to scale up the number of ion-qubits in a single trap and to explore many-body quantum models in two-dimension.[1–6] Recently, a fully-connected quantum computer has been realized with up to 5–20 ions forming 1D crystal in linear Paul traps[7,8] and over 50 ion-qubits have been used for a quantum simulation with restricted control.[9] Extra-dimension of the crystal can provide a quadratic scaling of the number of ion-qubits in the trap. Ion-qubits in the 2D crystal intrinsically has 2D laser-induced interactions, which facilitates studying 2D many-body physics through quantum simulation such as geometric frustration and topological phase of matter.[1–5]

The 2D ion-crystal can be naturally realized by using Penning trap. In the Penning trap that uses static magnetic field and dc voltages for the confinement, hundreds of ions form a rotating 2D crystal.[10] Effective Ising interactions among ion-qubits in the 2D crystal have been engineered,[11] and entanglement of spin-squeezing has been studied.[12] Due to a high magnetic field condition and the fast rotation of ions in Penning traps, however, no clock-state of an ion can represent an effective spin, and it is challenging to implement individual spin controls with laser beams.

Paul traps do not require high magnetic fields for confinement of ions and can be an alternative platform to implement 2D crystal. There have been deliberate proposals and experimental exertions to confine 2D ion crystals in the Paul trap.[4,5,13–28] The main difficulty in Paul trap for producing 2D crystal of ions for quantum computation or quantum simulation lies in the existence of micromotion[29] synchronous with the oscillating electric field that introduces phase modulations on laser beams for cooling and coherent operation. The micromotion can be nullified at a point or in a line, but not in a plane. To address the micromotion problem, arrays of micro traps have been proposed[13–19] and small scale of arrays traps have been implemented.[16–21] Due to relatively large distances between micro traps, however, the Coulomb-coupling strength between ion-qubits in different traps would be relatively weak and so the effective spin–spin interactions induced by laser beams of coherent operations.[30–32] Alternatively, it has been proposed to produce a trap, where the direction of micromotion is

Y. Wang, M. Qiao, Z. Cai, K. Zhang, N. Jin, P. Wang, W. Chen, C. Luan, B. Du, H. Wang, Y. Song, D. Yum, K. Kim
Center for Quantum Information
Institute for Interdisciplinary Information Sciences
Tsinghua University
Beijing 100084, P. R. China
E-mail: ye.wang2@duke.edu; kimkihwan@mail.tsinghua.edu.cn
Y. Wang
Department of Electrical and Computer Engineering
Duke University
Durham NC 27708, USA
K. Zhang
MOE Key Laboratory of Fundamental Physical Quantities Measurements
Hubei Key Laboratory of Gravitation and Quantum Physics
PGMF and School of Physics
Huazhong University of Science and Technology
Wuhan 430074, China
D. Yum
Department of Physics and Astronomy
Seoul National University
Seoul 08826, South Korea

The ORCID identification number(s) for the author(s) of this article can be found under https://doi.org/10.1002/qute.202000068

DOI: 10.1002/qute.202000068

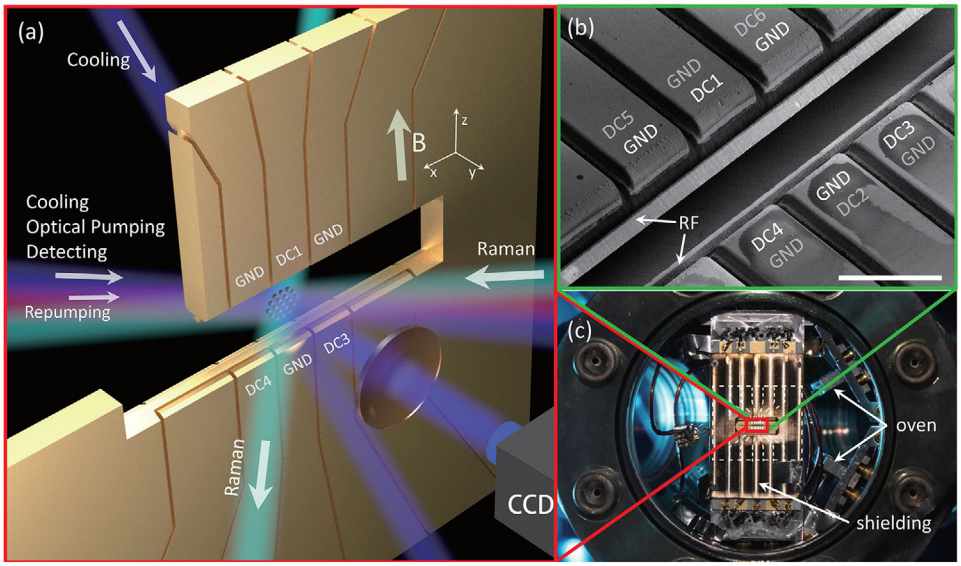

Figure 1. Trap structure and beam configuration. a) Conceptual drawing of our trap and the configuration of laser beams for cooling, pumping, detection (370 and 935 nm), and coherent operations (355 nm). The magnetic field is applied vertically. b) Scanning electron microscope (SEM) image of our trap (white scale bar, 400 μm). The trap structure is laser-machined on a single piece of alumina with less than 10 μm precision. Gold is electro-plated on the surface of alumina with 10 μm thickness. The trap has a total of 20 electrodes, where 14 of them are connected to GND and the others to DC sources. The gray letters label the electrodes on the opposite side of the trap. c) Image of our monolithic trap mounted in a hemi-sphere vacuum chamber. The trap is shielded with stainless steel plates on the front and back, respectively, which are connected to GND. The dashed lines show the electrodes underneath of the shield.

perpendicular to the net-propagation direction of laser beams for coherent control.[4,5] Such a trap structure is relatively simple to manufacture and can easily hold tens to hundreds of ions.

Here, we report the implementation of a Paul trap that confines tens of ions in a 2D crystal without disturbance of micromotions for quantum operations. The trap is monolithic, fabricated in a single piece of gold-coated alumina plate with the structure of the trap electrodes to precisely control the orientation of principle axis on the plane of the 2D crystal. This ensures perpendicularity between the micromotion axis and the net-propagation direction of Raman laser beams, which minimizes the effect of micromotion on coherent quantum operations. The 2D crystal is located on the plane composed of axial and one of transverse axes similar to that of linear-ion chains, where the imaging and individual manipulation systems are already well developed. With these developments, we are able to perform coherent operations on ions in the 2D crystal by using vibrational modes and the spectroscopy of vibrational modes of ten ions. Importantly, we observe that the amplitudes of micromotions in the 2D crystal are similar to that of a single ion by comparing the carrier and micromotion sideband transition-strengths with three ions. Our demonstration provides a solution to the important problem of how to realize a 2D-trapped-ion based quantum simulator and computer in a Paul trap.

2. Monolithic Trap: Design and Fabrication

We develop a Paul trap that can produce a pancake-like harmonic potential to trap the 2D crystal of ions and set the direction of micromotions on the plane of the 2D crystal. The trap is a 3D monolithic trap[33–35] constructed on a single layer of gold-plated laser-machined alumina[36,37] (see Appendix A). **Figure 1** shows the structure of our trap. In this structure, the 2D crystals of ions will be in the z–x place, which can be realized by squeezing the harmonic potential along y-axis, where the micromotion occurs along the z-axis. Here, the net-propagation direction of the Raman laser beam will be in the y-axis, which is perpendicular to the direction of micromotion. Therefore, the quantum operations by Raman laser beams will not be influenced by the micromotion.

The trap is functionally separated into three layers, where front and back layers contain dc electrodes, and the middle layer is used for RF electrode as conceptually shown in Figure 1a. The RF electrode has a slope with the angle of 45° relative to the normal direction of the alumina piece. In each DC layer, there are ten electrodes, five electrodes on both upside and downside with a 50 μm spacing. At the center of the trap, there is a 260 μm × 4 mm slot, where ions are trapped. The Figure 1b shows front side of the trap. The angle of the slope and the gap between DC and RF electrodes are optimized to maximize the trap frequency (see Appendix B). We use Charged Particle Optics (CPO) software to calculate the electric potential from the electrodes. We also compare the simulated potential with the real potential to calibrate the simulation coefficient for further trap simulation (see Appendix C). In the experiment, only six of twenty electrodes are connected to the stable DC sources, and the others to GND, as shown in Figure 1b.

The monolithic trap is located in a vacuum chamber shown in Figure 1c. The trap and vacuum system is designed to ensure sufficient optical accesses. $^{171}Yb^{+}$ ions are loaded to the middle of the trap by photo-ionization and Doppler cooling.[38] We create the 2D crystal of ions in a plane that consists of the axial axis (x-axis) and one of the radial axes (z-axis). We apply two

Doppler-cooling laser beams to couple all the three directions of ion motions, as shown in Figure 1a. The magnetic-field insensitive states of $^{171}Yb^{+}$ ion in the ground-state manifold $^2S_{1/2}$, $|F=0, m_F=0\rangle$ and $|F=1, m_F=0\rangle$ are mapped to qubit state $|0\rangle$ and $|1\rangle$, respectively. The state of the qubit is detected by the laser beam resonant to the transition between $F=1$ of $^2S_{1/2}$ and $F=0$ of $^2P_{1/2}$ and initialized to $|0\rangle$ by applying the optical pumping laser beam resonant with the transition between $F=1$ of $^2S_{1/2}$ and $F=1$ of $^2P_{1/2}$. The qubit is coherently manipulated by a pair of 355 nm picosecond pulse laser beams with beatnote frequency about the qubit transition $\omega_0 = 2\pi \times 12.642821$ GHz.

3. Rotation of Principle Axes

We demonstrate the capability of rotating the principle axes of the trap potential to ensure the micromotions to be on the 2D plane, which will be perpendicular to the net *k*-vector of Raman laser beams.[2,37] We rotate the principle axes in the *y*–*z* plane by adjusting voltages V_C and V_{NC} on both of the center electrodes DC_C (DC1, DC2 in Figure 1b) and all of the next to the center electrodes DC_{NC} (DC3, DC4, DC5, and DC6 in Figure 1b), respectively. The total pseudo-potential with voltages of V_C, V_{NC}, and V_{RF} is described by

$$\phi(x,y,z) = V_C\phi_C + V_{NC}\phi_{NC} + V_{RF}\phi_{RF} \quad (1)$$

where ϕ_C and ϕ_{NC} are electric potentials at the position of (x, y, z) generated by DC_C and DC_{NC} electrodes with unit voltage, and ϕ_{RF} is the pseudo-potential generated by the RF electrode with root-mean-square voltage of 1 V. In *y*–*z* plane, the symmetric RF pseudo-potential can be broken by DC potentials, which leads to a elliptical total potential $\phi(x,y,z)|_{x=0}$. The two axes of the elliptical potential are the principle axes. In order to rotate the principle axes to y axis and z axis, we need to satisfy

$$\partial\phi(0,y,\delta z)/\partial y|_{y=0} = 0 \quad (2)$$

where δz is the radius of a 2D crystal and small enough to be in harmonic regime for our consideration. In our numerical calculation, we use 30 μm for δz. Noticing $\partial\phi_{RF}(0,y,\delta z)/\partial y|_{y=0} = 0$ is always true, we can calculate the solution of V_{NC}/V_C, to satisfy Equation (2) based on numerical simulation. In our trap, $V_{NC}/V_C \approx 5.11$. We should also notice that whenever we set V_{NC}/V_C to the right value and rotate the principle axes to *y* axis and *z* axis, V_{RF} will no longer affect the rotation of the principle axes. Here, we do not consider the rotation of the principal axes along the *x*-direction in the small area near the trap center due to the transnational symmetry. Indeed, our numerical simulation also shows a negligible rotation of the principal axes up to $\delta x =$ 50 μm, which would introduce a micromotion disturbance similar to the level of intrinsic micromotion.

We numerically calculate ϕ_C, ϕ_{NC} and ϕ_{RF} with CPO software. We set the RF signal to be $\omega = 2\pi \times 40$ MHz and $V_{RF} = 80$ V. When $V_{NC}/V_C = \infty$ with $V_{NC} = 1.5$ V, vertical principle axis (green line in **Figure 2**a) is clockwise rotated by 22.9° from the *z*-axis. When the ratio $V_{NC}/V_C = 0$ with $V_C = 1.5$ V, the green axis is counter-clockwise rotated by 5.7° from the *z*-axis. As shown in Figure 2b, when the ratio $V_{NC}/V_C = 5.11$, the green axis is in line with *z*-axis.

We experimentally confirm the rotation of the principle axes in *y*–*z* plane with single ion by observing the disappearance of the Raman coupling to *z*-axis vibrational mode. The spectrum of vibrational modes, as shown in Figure 2c,d, is measured by the following procedure: 1) We perform Doppler cooling on ion-crystal, which results in thermal states with $\bar{n} \approx 7.1$ for mode frequency $\omega_y \approx 2$ MHz, and initialize the internal states to $|\downarrow\rangle$ by applying the standard optical pumping technique. 2) We apply Raman beams with a net *k*-vector perpendicular to the *z*–*x* plane. Once the beatnote-frequency ω_R of Raman beams matching to $\omega_0 \pm \omega_{y,z}$, sideband transitions occurs,[39] which can be detected by the fluorescence of ions that is collected by imaging system and photo-multiplier tube (PMT). In Figure 2c, the voltage ratio is close to the condition of $V_{NC}/V_C = \infty$ in Figure 2a, where the principle axes are tilted away from *y*–*z* axes. The net *k*-vector of Raman beams is along the *y*-axis, which can excite both directions of vibrational modes. Thus, two peaks in blue-sidebands ($\delta = \omega_{y,z}$) as well as red-sidebands ($\delta = -\omega_{y,z}$) are clearly visible in Figure 2c, where detuning $\delta = \omega_R - \omega_0$. However, when the principle axes are rotated to *y*–*z* axes as shown in Figure 2b, Raman beams cannot excite the vibrational mode along *z*-axis, which results in vanishing a peak in the Raman spectrum. Based on the spectrum of Figure 2d, we estimate that deviation of the principle axes from *y*–*z* axes is below 0.40°.

4. Loading and Imaging of 2D-Ion Crystals

In the Paul trap, there have been experimental observations of planar ion crystals.[16,17,20,21,23–28] We also create and observe 2D crystals in the plane of *z*–*x* axes. In order to produce a 2D ion crystal in the *z*–*x* plane, we need to satisfy $\omega_y > (2.264N)^{1/4}\omega_{x,z}$ (when $\omega_x = \omega_z$).[5,40] In general, we need four control parameters to rotate the principal axes and set three trap-frequencies independently. In the experiment, we find that three control voltages, V_C, V_{NC}, and V_{RF} in Equation (1), are enough to produce various geometries of the 2D crystals, which is only determined by the ratio of ω_x and ω_z when ω_y is large enough to be 2D crystals. First, keeping the principle axes to *y*–*z* axes, we can calculate the voltage solution for DC electrodes with a given axial trap frequency ω_x, which is mostly determined by V_{NC}. With determined DC potential, the relation between ω_y and ω_z is given by[39]

$$\omega_y^2 - \omega_z^2 = CV_{NC} \quad (3)$$

(see Appendix D) where *C* is a positive constant determined by the trap geometry. In the case of $V_{RF} = 0$, the *z*-axis potential, the shallower potential respective to that of the *y*-axis according to Equation (3), becomes anti-harmonic, which indicates $\omega_z^2 < 0$ and $\omega_y^2 < CV_{NC}$. On the other hand, since ω_y *and* ω_z monotonously increase with V_{RF}, there is a critical value of V_{RF} that makes $\omega_y^2 = CV_{NC}$ and $\omega_z^2 = 0$. Therefore, we can tune ω_y from $\sqrt{CV_{NC}}$ to ∞, ω_z from near zero to ∞ by tuning V_{RF}. As shown in Figure 2e, with different values of V_{RF}, we can have ω_z/ω_x from 0 to 2.72 for ten ions to realize 2D ion crystal with different aspect ratios.

Once the requirements of principle axes and trap-frequencies for 2D crystal are satisfied as discussed above, we can confine ions in the *z*–*x* plane. Fortunately, the strongest trap

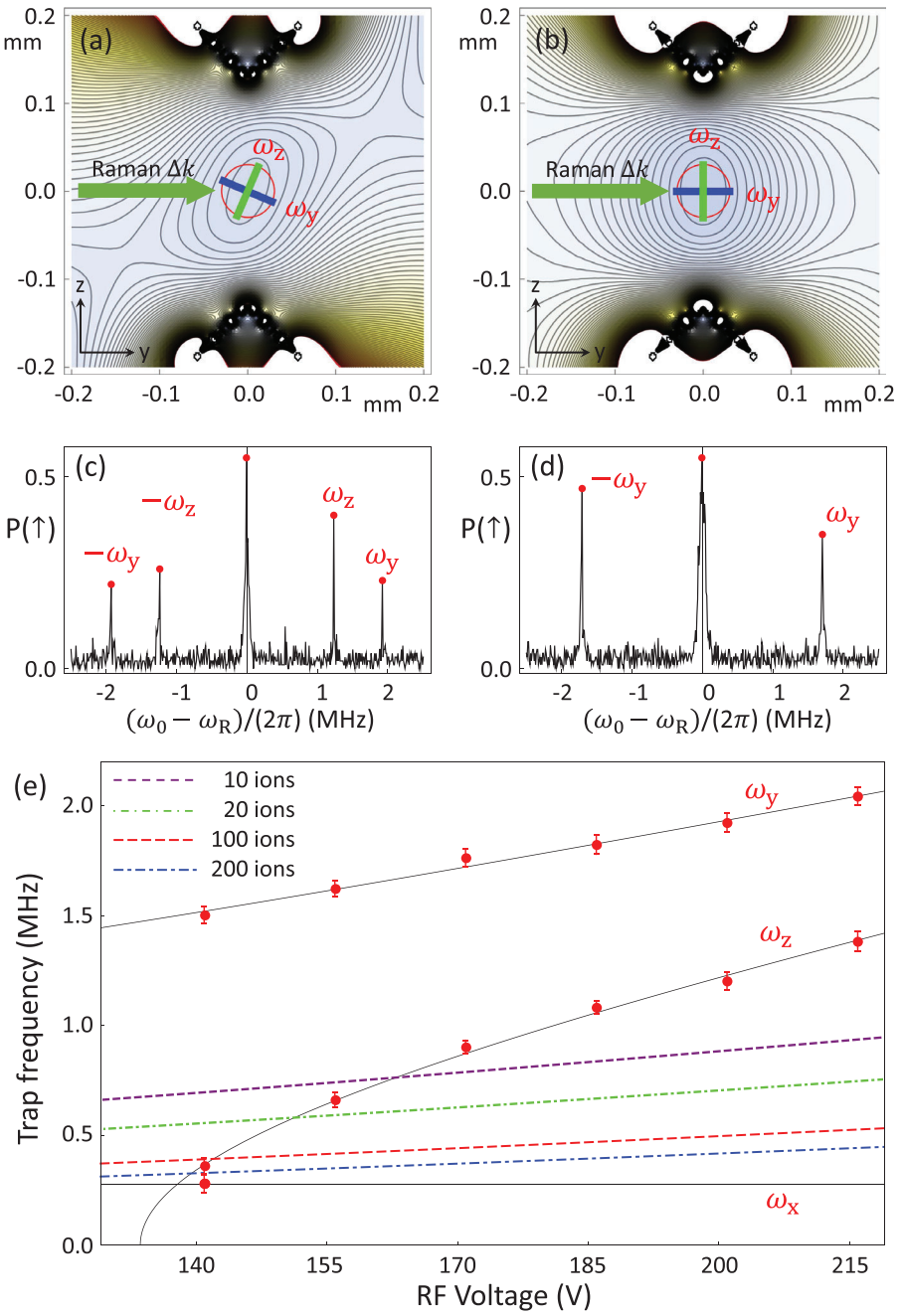

Figure 2. Principle axis rotation. a) The contour plot of pseudo-potential when $V_{NC}/V_C = \infty$, central electrodes are connected to GND. b) The contour plot of pseudo-potential when the principle axes are overlapped with *y* and *z* axes, where the voltage ratio is $V_{NC}/V_C = 5.11$. c) The Raman spectrum with principle axes in the condition of (a), where we can see both of the transverse modes. d) The Raman spectrum with principle axes in the condition of (b). In this situation, the Raman beams can only drive the mode of the *y*-axis, not that of the *z*-axis. e) Relation between two radial-mode frequencies and the RF voltages. By merely changing the RF voltage, we can realize different ratios of trap frequencies. The red dots are the experimental data; the dark lines are the fitting results. The error bar is the 3σ, where σ is the standard error representing the fitting errors. The dashed lines, which are calculated by $\omega_y/(2.264N)^{1/4}$ for different RF voltage, are the up bounds of the region where the symmetric 2D crystal can be formed for different numbers of ions.

frequency in our monolithic trap is in *y*-axis due to the geometry of the trap, which allows us to easily image the 2D crystal with the same imaging system to 1D chain. The fluorescence of ions in 2D crystal can be directly imaged through an objective lens to CCD camera as shown in Figure 1a.

Figure 3a shows the images of the 2D crystals and demonstrates the control capability for shapes of 2D crystals with various settings of trap frequencies. For the image of ten ions, the trap frequencies are $\{\omega_x, \omega_y, \omega_z\}/(2\pi) = \{0.427, 1.50, 0.561\}$MHz. For the image of 19 ions and 25 ions, the trap frequencies

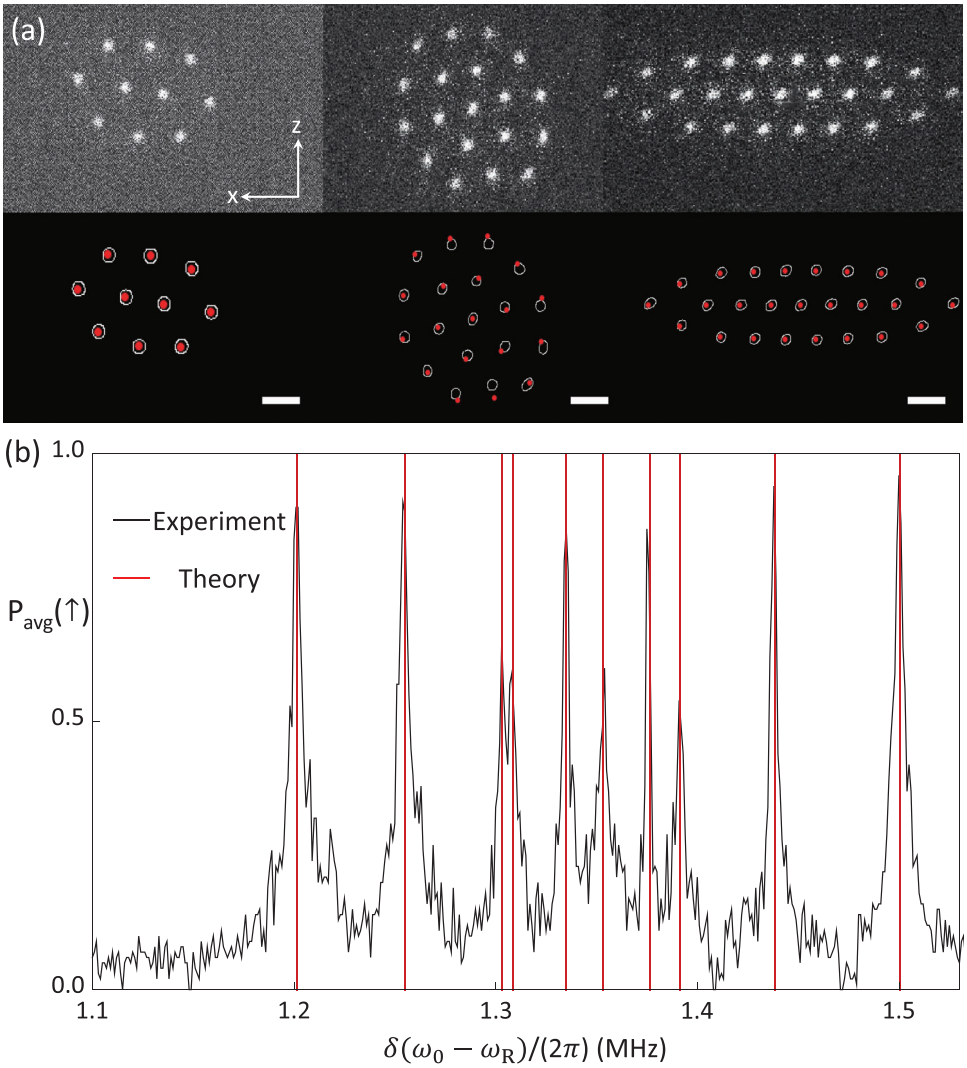

Figure 3. Geometry and mode structure of 2D-ion crystals. a) CCD images of 10-, 19-, and 25-ion crystals with different trap frequencies. The above ones are raw data taken from EMCCD, and the bottom ones compare the numerical simulation and the real data where the white cycles are the positions of ions read out from the CCD pictures and the red points are simulation results. The white scale bars represent 5 μm distance. b) Raman spectrum of the 2D crystal with ten ions. The crystal is first cooled by 1000μ s Doppler cooling; then a 3μ s optical pumping is performed to prepare the ground-state of qubits. The vibrational modes are excited by a 400μ s Raman sequence with 5 kHz Rabi frequency. The spectrum is obtained by collecting the fluorescence with PMT, and each data point is measured 100 times. The black curve is the experiment result, and the red lines are the theoretical prediction of the mode frequencies.[5]

are $\{\omega_x, \omega_y, \omega_z\}/(2\pi) = \{0.28, 1.50, 0.26\}$MHz and $\{\omega_x, \omega_y, \omega_z\}/(2\pi) = \{0.28, 1.63, 0.68\}$MHz, respectively. For 25 ions, the dashed line in Figure 2e is the upper bound of the ω_x and ω_z where the symmetric 2D crystal can be formed. However, for forming an asymmetry 2D crystal in Figure 3a, the criteria are complicated and have been discussed in refs.[28, 41]. We numerically study the situation in Appendix E. We can imagine an oblate ellipsoidal 3D crystal ($\omega_y > \omega_z = \omega_x$) whose in-plane trap frequencies are above the bound; then, if we reduce ω_x, the crystal will tend to 2D and finally results in a linear chain. The geometries of the crystal are in agreement with the numerical simulation. We simulate the geometry configuration of the ion crystal by numerically minimizing the electrical potential of the ions in a 3D harmonic trap.[5]

5. Raman Spectrum of Transverse Vibrational Modes of 2D Crystals

After loading the 2D crystals of ions, we drive the different transverse modes of a ten-ion crystal by varying the detuning between Raman beams, similar to the single ion case. Figure 3b shows the resulting spectrum, where each peak represents a motional mode in the y-axis. For the measurement, we first cool crystals to their vibrational ground-state via Doppler and EIT cooling, then apply the Raman beams to drive the motional sidebands. The measured mode spectrum is consistent with the theoretical simulation based on trap frequencies and geometry of 2D ion crystal.[5] The trap frequencies used for the simulation are $\{\omega_x, \omega_y, \omega_z\}/(2\pi) = \{0.427, 1.5, 0.561\}$MHz. We

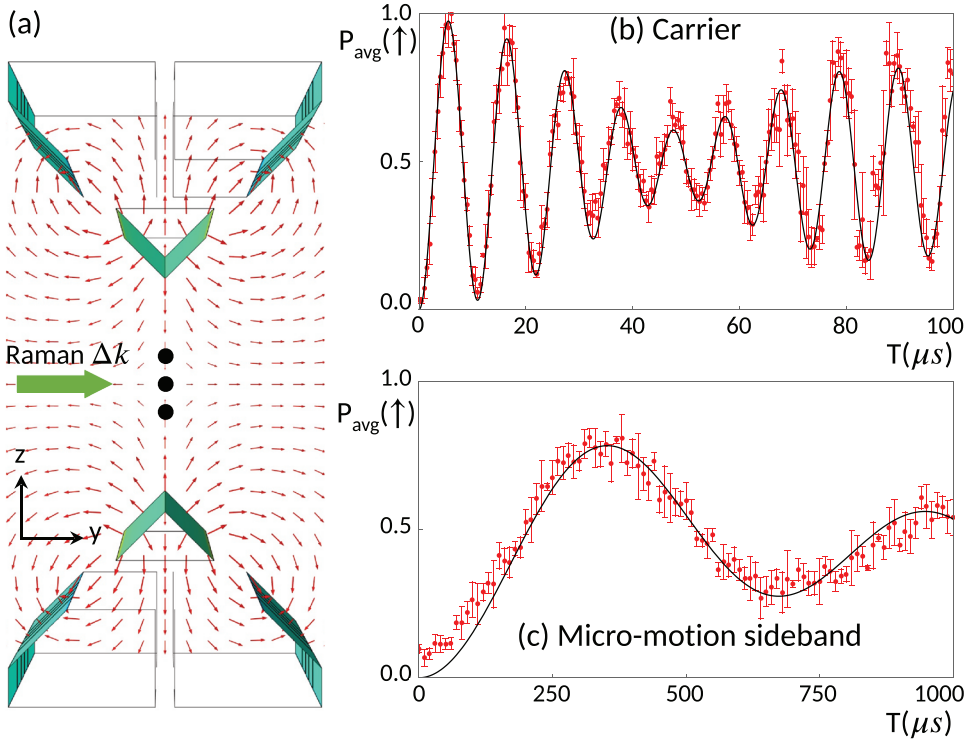

Figure 4. Micromotion direction and strength in the trap. a) Vector plot of the RF field is done by CPO. The simulation shows if the crystal is located in the *z*–*x* plane; the direction of micromotion is along the *z*-axis and perpendicular to the *y*-axis which is the net propagation direction of Raman beams. b) Carrier transition of three ions in triangular crystal. c) Micromotion transition of the three-ion crystal after compensating the micromotion. For (b) and (c), similar to Figure 3b, after 1000 μ s Doppler cooling, and 3 μs optical pumping, we apply Raman laser beams with the frequency differences of a) carrier transition and b) micro-motion sideband transition (separated by 40 MHz from the carrier) and collect the total fluorescence of all three ions by PMT. The beating signal comes from the unbalanced Rabi-frequency of each ion. Error bars denote the standard deviation of project measurements with repetition of 100 times.

directly measure the trap frequencies along the *y*-axis and the *x*-axis, and the trap frequency along the *z*-axis is used as a fitting parameter. The agreement between the experimental data and the pseudo-potential simulation shows that the micromotion induced shift is negligible in our system, different to the situation in ref.[26], where the full time-dependent potential including micromotion is required to fit the experimentally measured secular trap frequencies of 2D ion crystals. We also numerically simulate the amplitude of micromotion for each ion,[6] and estimate a maximal micromotion-induced frequency shift of 930 Hz.[5] Similar to the linear chain case,[42–46] when the phase transition from a 2D crystal to a 3D crystal happens, the minimal frequency of the modes along the *y*-axis will tend to be negative. Our measured mode frequencies are far away from zero, which provides an additional confirmation of 2D crystals of ions.

6. Compensation and Quantification of Micromotion in 2D Crystals

Ideally, if the crystal is located in the *z*–*x* plane, the direction of micromotion is along the *z*-axis and perpendicular to the *y*-axis, which is the net propagation direction of Raman beams as shown in **Figure 4**a. In practice, there are two possible imperfection sources that make the crystal deviate from the ideal micromotion condition: 1) stray electric field, which induces displacement; 2) fabrication imperfection of the electrodes, which induces the tilt around the *z*-axis. To minimize the micromotion from theses sources, we first compensate the straight field with a single-ion, then mitigate the tilt errors by slightly rotating the crystal. With the single ion, the micromotion compensation is done by overlapping the position of the ion to the null point of the RF electric field.[29] We first compensate the extra-field in *z* direction by changing the voltage of {DC2, DC3, DC4} or {DC1,DC5,DC6} simultaneously with the ratio {1, 5.11, 5.11}, which is able to keep the principle axes direction and avoid generating the displacement along *y* axis. We can also change the voltage of electrodes {DC1,DC3,DC4} or {DC2,DC5,DC6} with ratio {1, 5.11, 5.11} to compensate the extra-field in *y* direction. For the *z*-axis compensation, we minimize the change of ion position depending on RF power and for the *y*-axis compensation, we minimize the micromotion sideband transition of Raman beams. For the error induced by the fabrication imperfection, we slightly change the voltage of electrodes {DC3,DC4,DC5,DC6} with ratio {1, 1, 1, 1} to rotate the crystal around *x* axis and with ratio {1,-1,1,-1} to rotate the crystal around *z* axis. With the control, we also minimize the Rabi-frequency of the micromotion sideband transition with three ions.

The strength of the micromotion is quantified by measuring the ratio between two Rabi frequencies of the carrier (Figure 4b) and the micromotion transition (Figure 4c).[29] We measure the

micromotion strength in a three-ion 2D crystal. We first sequentially apply Doopler cooling and EIT cooling[47] to cool the 2D crystal down to near the motional ground-state. Then, we drive the Rabi flopping and measure the Rabi frequency of the carrier and the micromotion sideband transition. For each flopping, we collect the overall counts of three ions with PMT and fit the result with three Rabi frequencies. Note, that the variation of Rabi frequencies due to micromotion has been used for individual addressing single ions in a crystal.[48] The fitting gives us three carrier π-time {5.96, 5.40, 5.19}μs and three micromotion sideband π-time {474, 440, 317}μs. The modulation index, which is given by $\beta/2 = \Omega_{\text{micro}}/\Omega_{\text{carrier}}$, has a maximun possible value of 0.038 and a minimal possible value of 0.021, which are similar to single ion situations.

7. Coherent Operations on the Vibrational Sidebands of 2D Crystals

After minimizing the strength of the micromotion, we demonstrate coherent manipulations of collective motional modes along y-axis for a three-ion 2D crystal. Three frequencies of the motional modes are $\omega_{y1}/(2\pi) = 1.33$ MHz, $\omega_{y2}/(2\pi) = 1.27$ MHz, and $\omega_{y3}/(2\pi) = 1.21$ MHz. Three ions form a isosceles triangle with an apex angle of 260.7 degrees. To observe the evolution more clearly, we only collect fluorescence of the center ion, which is at the apex angle, by PMT in this experiment. We first cool the crystal to motional ground-state via 1000μ s Doppler cooling and 200μ s EIT cooling; then after 3μ s optical pumping, we globally apply Raman beams on three ions and drive a blue-sideband transition for the coherent manipulation. Our blue-sideband transition induces additional off-resonant couplings to other motional modes. The Hamiltonian is written as

$$H = -\frac{i\eta}{2}\sum_{i=1}^{3}\sum_{j=1}^{3}\Omega^{(j)}b_i^{(j)}\sigma_+^{(j)}a_i e^{-i\delta_i t} + \text{H.C.} \tag{4}$$

where η is the Lamb–Dicke parameter of a single ion, $\Omega^{(j)}$ and $\sigma_+^{(j)}$ are the carrier Rabi frequency and spin raising operator for the j^{th} ion, $b_i^{(j)}$ $(j = 1, 2, 3)$ characterizes the i^{th} normalized mode vector of the collective mode,[49] a_i is the annihilation operator for the i^{th} motional mode, and $\delta_i = \omega_L - \omega_0 - \omega_{yi}$ where ω_L is the frequency of the Raman beat-note. **Figure 5**a shows the carrier Rabi flopping for the center ion, which leads to $\Omega^{(2)}/(2\pi) =$ 57.6 kHz. Figure 5b shows the Rabi flopping data when we drive the laser resonant with the zig-zag mode, that is, $\omega_L = \omega_0 + \omega_{y3}$. The black lines in Figure 5c are the simulation results with parameters as $\Omega^{(1)} = \Omega^{(2)} = \Omega^{(3)} = 57.6$ kHz, $\eta = 0.108$, and $b_i^{(j)} =$ {{0.577,0.577,0.577},{0.707,0,-0.707 },{0.408,0.816,-0.408}}. The time evolution of the Hamiltonian shown in Equation (4) is complex, especially considering the off-resonant couple to other two motional modes. If we do not include such off-resonant couplings, the simulation is seriously deviated from the experimental data shown in black-dashed line of Figure 5b. The good agreement between red points and black line in Figure 5b indicates reliable coherent manipulation and the negligible micromotion effect during the coherent operation. We also numerically study the time evolution in the basis of the quantum states, which indicates it is a coherent evolution that $|000\rangle|n=0\rangle$ and $|101\rangle|n=2\rangle$ are mainly involved (detailed discussions in Appendix F and Figure F1).

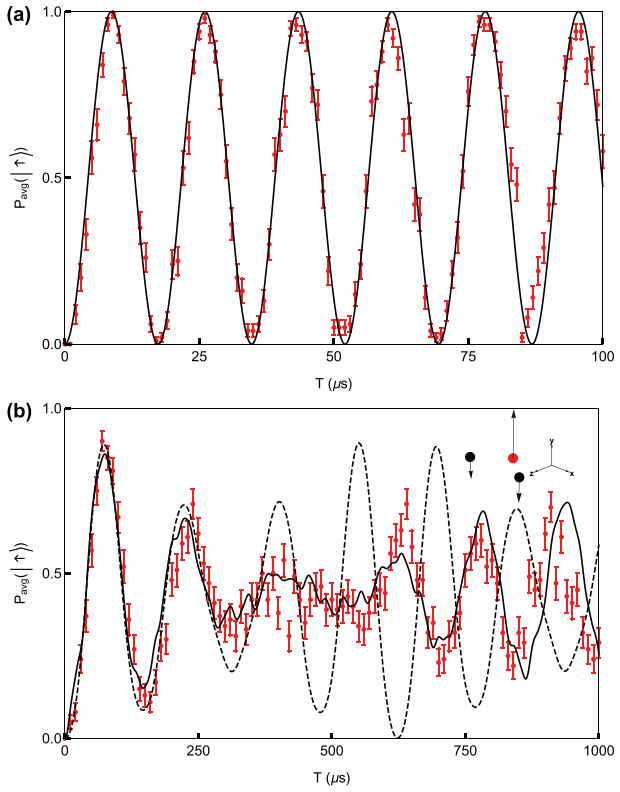

Figure 5. Coherent dynamics in a three-ion 2D crystal. a) Carrier Rabi oscillation. b) Rabi oscillation for the blue sideband transition on the zig-zag mode. Error bars denote the standard deviation of project measurements. Here, all the data are taken with a three-ion 2D crystal, which forms an isosceles triangle with an apex angle of 260.7 degrees. We only collect the fluorescence of the center ion at the apex angle, which is highlighted in the ionic structure schematic. The crystal is first cooled by a 1000μ s Doppler cooling, then is cooled to ground-state through a 200μ s EIT cooling. After a 3μ s optical pumping, the Raman beams are applied to the crystal to drive blue-sideband transition of the zig-zag mode. Red points are the experimental data. Error bars are the standard deviations. Black lines are the simulation results including all three motional modes. The dashed black line is the simulation result without considering off-resonant coupling to other two motional modes. Here, the mode frequencies are $\omega_{y1}/(2\pi) = 1.33$ MHz, $\omega_{y2}/(2\pi) = 1.27$ MHz, and $\omega_{y3}/(2\pi) = 1.21$ MHz. For both carrier and sideband oscillation, experimental sequences are repeated 100 times.

We also experimentally study the heating of the vibrational modes in our trap with a single ion. We first prepare the ground-state of radial vibrational modes by Raman-sideband cooling, wait for a certain duration, and measure average phonon-number $\bar{n}$ for the mode of interest. We estimate $\bar{n}$ by Fourier transforming the blue-sideband transitions.[39] We find that the heating rate of y-axis mode with the principle axes of 2D crystal (Figure 2b) is around 670 quanta per second, which is about 4.65 times larger than that with the condition of Figure 2a. It is understandable, since the noise of environmental electric field along y-axis would be more severe than those of the other axes.

8. Conclusion and Outlook

Our trap can be considered as an exemplary platform for implementing various proposals of quantum simulations with 2D crystal.[1–5] It can be used to observe a structural quantum phase transition from 2D to 3D with relaxed requirements.[50] Incorporating the capability of individual control and detection, universal quantum computation also can be achieved with more number of qubits than in a linear chain. The capability of laser addressing in a 2D space has been demonstrated with different techniques.[51,52] The detection of individual ions already has been well established using camera with high detection efficiency.[53]

Furthermore, the 2D crystal may be a natural platform for the fault-tolerant quantum computation schemes with 2D geometry, including the surface code,[54] the Bacon-Shor code,[55] and the (2+1) dimensional fault-tolerant measurement-based quantum computing.[56–58] Even though the full connectivity of trapped-ion system provides the capability of implementing any fault-tolerant scheme without extra overhead at the circuit level,[59–61] with a 2D ion crystal, the locality of 2D topological codes can be implemented, without mapping them code on a 1D ion chain, which comes at the expense of gates between ions at a distance or shuttling of ions.

Appendix A: Fabrication Process

The substrate is a single piece of alumina with a thickness of 380 μm and a surface flatness of less than 30 nm. The electronic structure is fabricated by the laser-machining and coated with 3 μm gold by electroplating technology. The detailed procedure to fabricate the electrodes structure is as follows: 1) Carve a slot of 260 μm at the center of the piece, as shown in **Figure 1**a; 2) make a slope of 45° on each side by cutting small steps to fit the slope as shown in Figure 1b; 3) make a tiny groove on each slope. The width of the groove is around 50 μm; 4) do gold coating on both sides of the chip as shown in Figure A1; 5) cut deeper in the groove position to remove gold. The center layer is electrically separated with top and bottom layer; 6) laser cut the slots on top and bottom layer to electrically separate all DC electrodes. Among all the steps, the second is the subtlest one. The geometry of the four slopes is crucial for the ion control with DC voltages. In step (2), for each slope, we apply 40 times of laser cutting with different duration and 5 μm shift on cutting position. The cutting duration for each pulse is calculated based on the calibrated relationship between the cutting depth and the cutting time. The laser cutting precision is ±1 μm, which is limited by the worktable instability. Using a laser with a power of 2 W, a wavelength of 355 nm, and a beam waist of around 15 μm, we can have the cutting speed to be 100 mm s^{-1}.

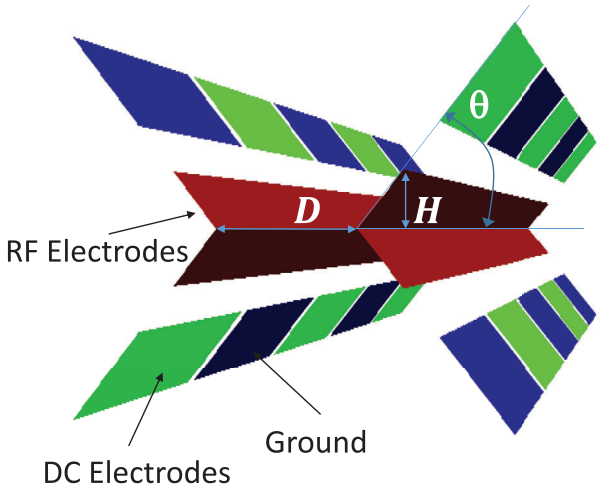

Figure A1. Steps for fabricating the structure of electrodes. a) Laser cut the 260 μm slot. b) Cut 40 small steps for each slope with 45°. c) Laser cut the small groove and electroplate gold on the surface. d) Cut the slots on the grooves and two sides of the chip to electrically separate all DC and RF electrodes.

Appendix B: Structure of the Trap

We use CPO software to simulate the trap performance with various geometric parameters. There are three important parameters for the trap design: the distance between two RF electrodes D, the height of RF electrodes H, and the angle of the slope θ as shown in **Figure B1**. We optimize these three parameters mainly to achieve large secular frequencies in the radial direction given fabrication limitation. The secular frequency is approximately inversely proportional to D^2,[39] which is inspected in our numerical simulation. We balance the requirement of large trap frequency and low UV-light scattering, which leads to the choice of $D = 260$ μm. For the slope angle θ, our simulation shows the best performance at $\theta \approx 47°$. Due to the fabrication difficulty of the angle, we choose $\theta = 45°$. Our simulation shows the best value of H is around 30 μm. Considering the laser cutting precision, we decide $H = 40$ μm.

Appendix C: Trap Simulation Calibration

Due to the fabrication imperfection, the real trap potential may deviate from the ideal model in simulation. We develop a method to quantitatively calibrate difference between the reality and the simulation, which is useful for the further simulation and the prediction of the trap behavior. Take $\phi_C(x, 0, 0)$ as an example; we can describe difference between the reality and the simulation as follows:

$$\phi_{\text{real,C}}(x, 0, 0) = \eta_{\text{C},x}\phi_{\text{sim,C}}(x, 0, 0) \tag{C1}$$

where $\phi_{\text{real,C}}(x, 0, 0)$ is the real potential generated by electrode DC_C along the x-axis, $\phi_{\text{sim,C}}(x, 0, 0)$ is the simulated potential, and $\eta_{\text{C},x}$ is the imperfection coefficient for DC_C in x-axis. We study the relationship between the real axial trap frequency and the simulated axial trap frequency to calibrate $\eta_{\text{C},x}$.

We start from calculating the axial mode frequency, which is $\omega_x = \sqrt{\partial^2\phi(x, 0, 0)/\partial^2 x}|_{x=0}$. By using the expression of ϕ in Equation. (1), we can have

$$\omega_x^2 = V_\text{C}\frac{\partial^2\phi_\text{C}(x, 0, 0)}{\partial^2 x} + V_\text{NC}\frac{\partial^2\phi_\text{NC}(x, 0, 0)}{\partial^2 x}|_{x=0} \tag{C2}$$

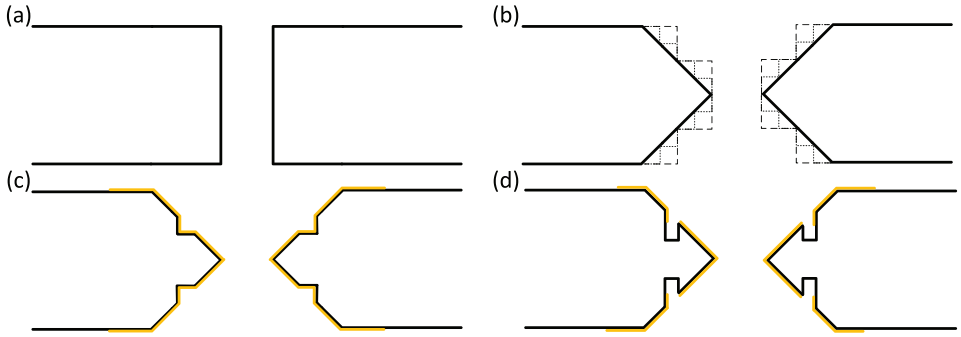

Figure B1. Important geometric parameters for the trap design . We generate 3D models with all combinations of three parameters and calculate the pseudo-potential and the secular frequency with CPO software. Maximizing the secular frequencies given fabrication limitation and laser-light scattering, we choose $D = 260$ μm, $\theta = 45°$, and $H = 40$ μm for the trap.

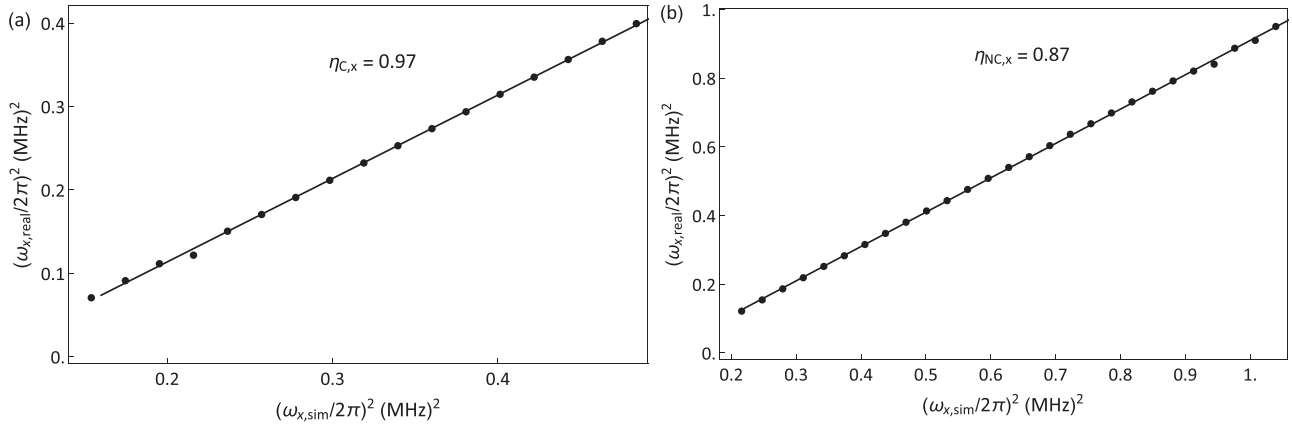

Figure C1. Axial potential calibration. a) We only change the value of V_{NC} and measure $\omega_{real,x}$. Then, we simulate the ideal $\omega_{sim,x}$ using the same DC voltage condition. By linear fitting the points $\{\omega^2_{x,real}, \omega^2_{x,sim}\}$, we can get $\eta_{NC,x} = 0.87$. b) We only change the value of V_C and plot all the points $\{\omega^2_{x,real}, \omega^2_{x,sim}\}$. By linear fitting the points, we can get $\eta_{C,x} = 0.97$.

With the Equation (C2) and fixed value of V_{NC}, we can treat ω_x^2 as a linear function with V_C, which has the slope as $a = \frac{\partial^2\phi_C(x,0,0)}{\partial^2 x}|_{x=0}$ and the intercept as $b = V_{NC}\frac{\partial^2\phi_{NC}(x,0,0)}{\partial^2 x}|_{x=0}$. We can write two versions of Equation (C2)

$$\omega^2_{x,real} = a_{real} V_C + b_{real} \tag{C3}$$

$$\omega^2_{x,sim} = a_{sim} V_C + b_{sim} \tag{C4}$$

where

$$a_{real} = \frac{\partial^2\phi_{real,C}(x,0,0)}{\partial^2 x} \tag{C5}$$

$$a_{sim} = \frac{\partial^2\phi_{sim,C}(x,0,0)}{\partial^2 x} \tag{C6}$$

So we know

$$\eta_{C,x} = \frac{\phi_{real,C}(x,0,0)}{\phi_{sim,C}(x,0,0)} = \frac{a_{real}}{a_{sim}} \tag{C7}$$

Combining Equations (C3), (C4), and (C7), with the same value of V_C, we can have

$$\omega^2_{x,real} = \eta_{C,x}\omega^2_{x,real} + b_C \tag{C8}$$

where b_C is an intercept determined by V_{NC} and geometries of other electrodes. We measured axial trap frequency $\omega_{x,real}$ by adding a modulation signal on one of the DC electrodes and checking the ion image. When the modulation frequency is close to the axial mode frequency, the motion of the ion is resonantly excited and melting in the axial direction. By changing V_C and plotting the points $\{\omega^2_{x,real}, \omega^2_{x,sim}\}$ in **Figure C1a**, we can fit the coefficient of $\eta_{C,x} = 0.97$. By doing same measurement but only changing V_{NC}, we can obtain $\eta_{NC,x} = 0.87$. $\eta_{C,x}$ is close to 1, which means the geometry of the center electrodes is near perfect in the axial direction. On the other side, $\eta_{C,x} = 0.87$ indicates that DC_{NC} electrodes are further away from the ion in the reality than in the

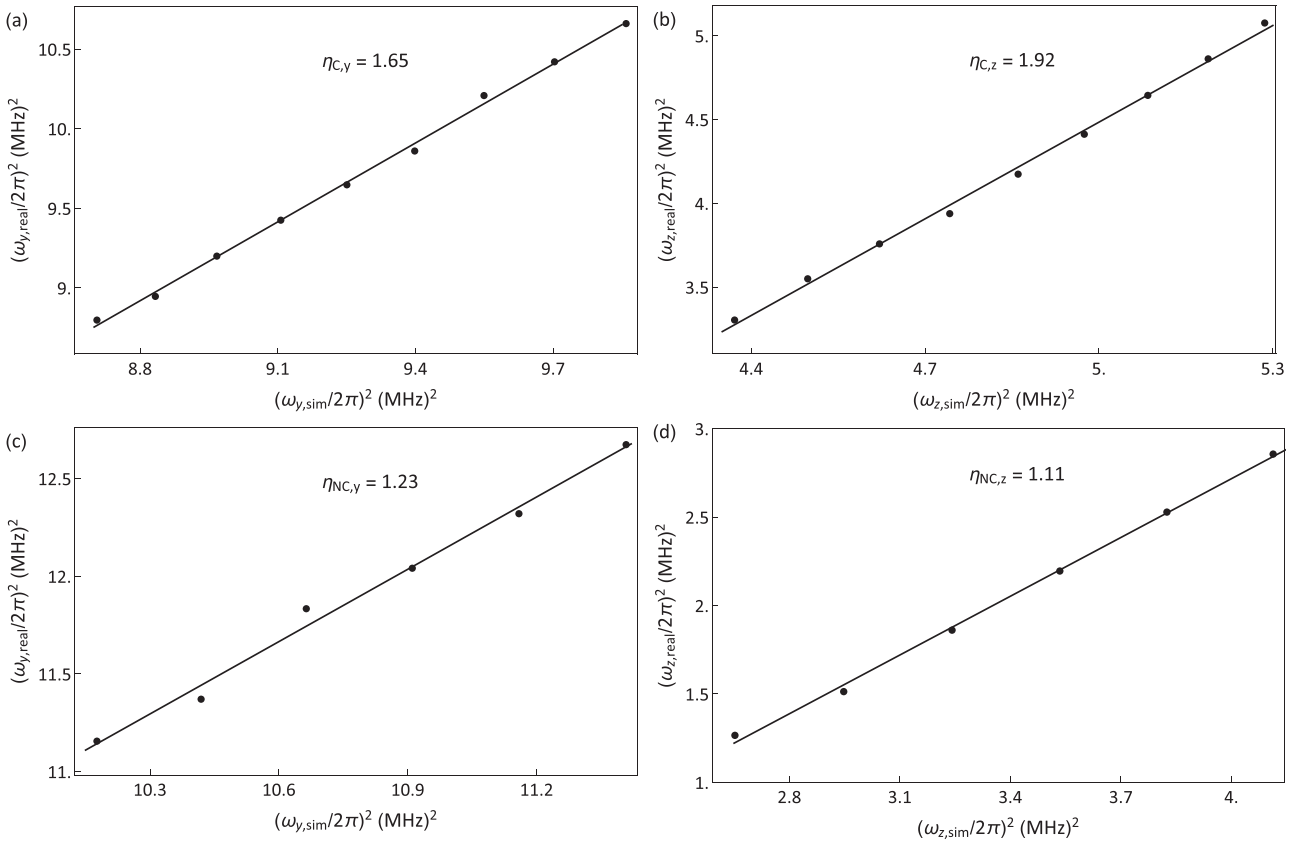

Figure C2. Radial potential calibration. a) We only change the value of V_C and measure $\omega_{real,y}$. Then, we simulate the ideal $\omega_{sim,y}$ using the same DC voltage condition. We check the rotation of the principle axes in the experiment and in the simulation to ensure the approximation assumption. By linear fitting the points $\{\omega^2_{x,real}, \omega^2_{x,sim}\}$, we can get $\eta_{C,y} = 1.65$. With the same procedure in (b)–(d), we calibrated the imperfection factor $\eta_{C,z} = 1.92$, $\eta_{NC,y} = 1.23$, and $\eta_{NC,z} = 1.11$

simulation. Whenever we want to simulate the axial potential, we need to include $\eta_{C,x}$ and $\eta_{NC,x}$ in consideration.

To calibrate the imperfection coefficients of two radial principle axes, y-axis and z-axis, we execute the same procedure as the axial calibration with more careful consideration about the principle-axes rotation. During the process of changing V_{NC} or V_C, only if we keep the rotation angle of the principle axes in a small regime, we can have the similar equations as Equation (C8) for y-axis and z-axis:

$$\omega^2_{y,real} \approx \eta_{C,y}\omega^2_{y,real} + b_{C,y} \tag{C9}$$

$$\omega^2_{z,real} \approx \eta_{C,z}\omega^2_{z,real} + b_{C,z} \tag{C10}$$

$$\omega^2_{y,real} \approx \eta_{NC,y}\omega^2_{y,real} + b_{NC,y} \tag{C11}$$

$$\omega^2_{z,real} \approx \eta_{NC,z}\omega^2_{z,real} + b_{NC,z} \tag{C12}$$

All the data are shown in **Figure C2**. From the data and the linear fitting, we can obtain $\eta_{C,y} = 1.65$, $\eta_{C,z} = 1.92$, $\eta_{NC,y} = 1.23$, and $\eta_{NC,z} = 1.11$. All these imperfection coefficients are larger than 1, which indicates that all, relative to the ideal model, the DC electrodes are closer to the ion in the radial direction in the reality. When we simulate the radial potential and check the principle axes rotation in the yz-plane, we use the average value $\eta_{C,yz} = 1/2(\eta_{C,y} + \eta_{C,z}) = 1.785$ and $\eta_{NC,yz} = 1/2(\eta_{NC,y} + \eta_{NC,z}) = 1.17$ to be the coefficients multiplied to $\phi_C(0, y, z)$ and $\phi_{NC}(0, y, z)$.

Appendix D: Trap Frequency Calculation

According to ref.[39], we can write the time-dependent potential of the trap as follows:

$$\phi(x, y, z, t) = \sum_{E\in DC} \frac{1}{2} V_E(\alpha_E x^2 + \beta_E y^2 + \gamma_E z^2) + V_{RF}\cos(\omega_{RF} t)(\alpha' x^2 + \beta' y^2 + \gamma' z^2) \tag{D1}$$

where V_E is the voltage applied on the DC_E electrode; α_E, β_E, γ_E are geometric factors determined by the geometry of the DC_E electrode; V_{RF} is the root mean square of the voltage applied on RF electrode; α', β', and γ' are geometric factors determined by the geometry of the RF electrode. We note that x, y, and z axes in Equation (D1) should be three principle axes of the trap

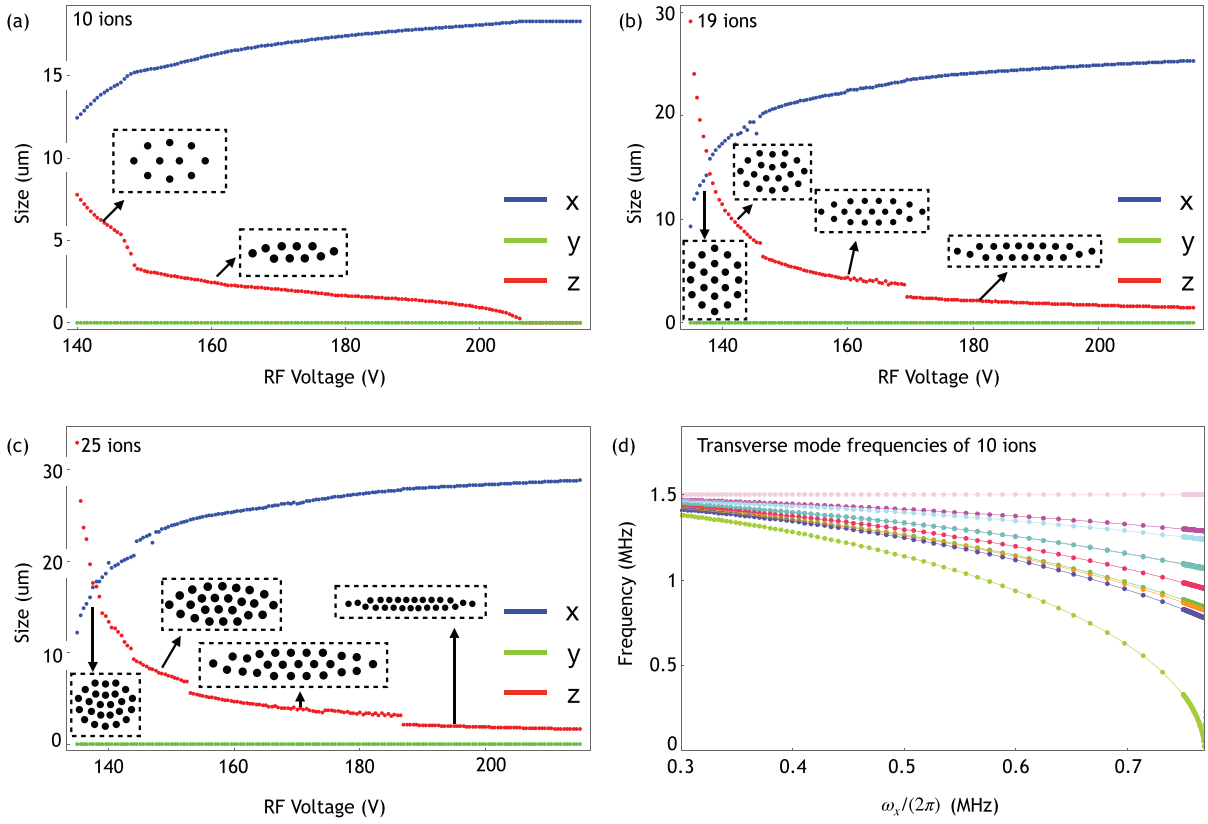

Figure E1. Simulation of geometry and mode frequencies (a–c). The relation between crystal size and the RF voltage for the cases of 10, 19, and 25 ions. Here, we define the size of crystal as the maximal coordinate difference in the *x*, *y*, or *z* axes among the ions. The zero value of the crystal size along the *y*-axis shows the crystal is confined in 2D on the *x*–*z* plane, and when the size of *z* axis becomes zero, the ions form a linear chain. The sudden jumps of the crystal size indicates a structure phase transition. d) If we squeeze the 10-ion crystal in the *z*-*x* plane by increasing *wx* and *wz* while keeping the ratio as $wx/wz = 1.3$, the frequency of the motional modes along the *y*-axis will become broader, and once the minimal frequency meet zero, a phase transition from 2D to 3D happens.

potential. All the geometric factors will change based on the different rotation of the principle axes. The condition that the potential has to fulfill the Laplace equation $\Delta\Phi = 0$ leads to the restrictions as follows:

$$\alpha + \beta + \gamma = 0 \tag{D2}$$

$$\alpha' + \beta' + \gamma' = 0 \tag{D3}$$

With our symmetric RF electrodes in the axial direction, it is clear that $\alpha' = 0$, which leads to $\beta' = -\gamma'$. Solving the Mathieu equation for three directions, we can have the results as follows:

$$\omega_x = \sqrt{\frac{4e\sum_{E\in DC} V_E \alpha_E}{m\omega_{RF}^2} + \frac{2e^2 V_{RF}^2 \alpha'^2}{m^2\omega_{RF}^4}}\frac{\omega_{RF}}{2} \tag{D4}$$

$$\omega_y = \sqrt{\frac{4e\sum_{E\in DC} V_E \beta_E}{m\omega_{RF}^2} + \frac{2e^2 V_{RF}^2 \beta'^2}{m^2\omega_{RF}^4}}\frac{\omega_{RF}}{2} \tag{D5}$$

$$\omega_z = \sqrt{\frac{4e\sum_{E\in DC} V_E \gamma_E}{m\omega_{RF}^2} + \frac{2e^2 V_{RF}^2 \gamma'^2}{m^2\omega_{RF}^4}}\frac{\omega_{RF}}{2} \tag{D6}$$

Due to $\beta' = -\gamma'$, we can have

$$\omega_y^2 - \omega_z^2 = \frac{e}{m}\left[\sum_{E\in DC}(\beta_E - \gamma_E)V_E\right] \tag{D7}$$

This equation explains Equation (3). As we mentioned before, all the geometric factors are determined by the rotation of the principle axes.

Appendix E: Geometry of Ion Crystal and Simulation of Mode Frequencies

We calculate the dashed lines in Figure 2e using the formula $\omega_y/(2.264N)^{1/4}$,[5] where ω_y varies with the RF voltage. When ω_x and ω_z are both bigger than $\omega_y/(2.264N)^{1/4}$, the ions form a 3D crystal. When ω_x and ω_z are both smaller than the bound, the ions form a 2D crystal. However, when two frequencies are not larger

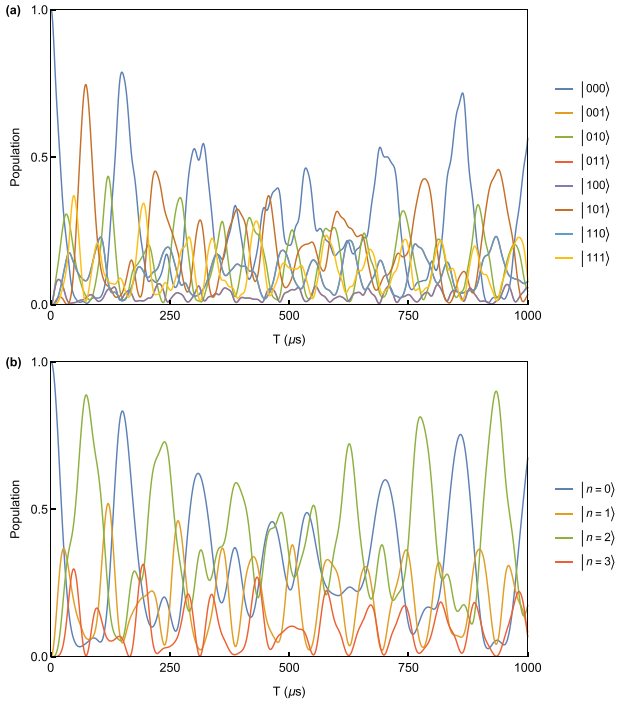

Figure F1. Simulations of time evolution for internal and motional states in a three-ion 2D crystal. a) The time evolution for eight internal states after tracing out motional states. Due to the symmetric between two side ions, the evolution of states |001⟩ and |100⟩ and |011⟩ and |110⟩ are identical. b) The time evolution for the zig-zag mode in phonon number basis after tracing out internal states. The occupied phonon state is bounded to $|n = 3\rangle$ as the characteristic of three-ion blue-sideband transition.

or smaller than the bound at the same time, there is no simple expression of the critical point for the phase transition from a 2D crystal to a 3D crystal. For example, if one of the modes is below the bounds while the other above, the ions can still form a 2D crystal. We can imagine such a situation from a homogeneous crystal where $\omega_x = \omega_z > \omega_y/(2.264N)^{1/4}$. In this case, the ions form a 3D crystal not 2D, but if we release the confinement along the *x*-axis by lowering ω_x, at a certain ω_x, the ions can form a 2D crystal. We verify this situation for 10, 19, and 25 ions by numerically simulating the equilibrium positions of the ions and study the structures of the crystals if they are in 2D, as shown in **Figure E1**. Here, we simulate the geometry of crystals by minimizing the pseudo-potential of the crystal at zero temperature. Compared with the molecular dynamics simulation, including oscillating fields, the pseudo-potential solution has a shifted critical point,[62,63] while the overall structure is similar.[5,26] The critical point of the structure phase transition can be calculated more precisely by mapping it to the six-state clock model,[41] and including the effect of finite temperature and quantum fluctuations.[41]

As mentioned in the main text, in the region near the phase transition from 2D to 3D, the minimal frequency of the transverse modes will tend to zero. We also numerically study this behavior on a ten-ion 2D crystal and show the result in Figure **E1d**.

Appendix F: State Evolution in a Three-Ion 2D Crystal When Driving the Zig-Zag Mode

We numerically simulate the coherent dynamics for the blue-sideband transition on zig-zag mode shown in Figure 5b with the the Hamiltonian shown in Equation (4). **Figure** F1a shows the simulation of time evolution for three internal states after tracing out motional states. The time evolution is complex, especially considering all the off-resonant couple to other two motional modes. However, we can clearly see that it is a coherent evolution. The initial state |000⟩ is mostly transferred to |101⟩ at around 75 μs and is returned at around 150 μs. Even longer evolution of around 860 μs, the |000⟩ state coherently comes back, which is strongly indicated in the experimental date of Figure 5b. Figure **F1b** shows the simulation of time evolution for motional states of zig-zag mode after tracing out internal states. The occupied phonon state is bounded to $|n = 3\rangle$ due to the characteristic of three-ion blue-sideband transition. Here, we find the dominant motional dynamics occurs between $|n = 0\rangle$ and $|n = 2\rangle$ states. The $|n = 2\rangle$ is mostly associated with |101⟩ state, which can be understood from the motional mode vector of the zig-zag mode.

Acknowledgements

Y.W. and M.Q. contributed equally to this work. The authors thank Jincai Wu and Haifeng Zhu at Interstellar Quantum Technology (Nanjing), Ltd. for many useful discussions on fabrication technique. This work was supported by the National Key Research and Development Program of China under Grants No. 2016YFA0301900 and No. 2016YFA0301901 and the National Natural Science Foundation of China, Grants No. 11374178, No. 11574002, and No. 11974200.

Conflict of Interest

The authors declare no conflict of interest.

Keywords

ion traps, quantum simulations, two-dimensions

Received: June 24, 2020
Revised: September 6, 2020
Published online:

[1] A. Bermudez, J. Almeida, F. Schmidt-Kaler, A. Retzker, M. B. Plenio, *Phys. Rev. Lett.* **2011**, *107*, 207209.
[2] A. Bermudez, J. Almeida, K. Ott, H. Kaufmann, S. Ulm, U. Poschinger, F. Schmidt-Kaler, A. Retzker, M. Plenio, *New J. Phys.* **2012**, *14*, 093042.
[3] R. Nath, M. Dalmonte, A. W. Glaetzle, P. Zoller, F. Schmidt-Kaler, R. Gerritsma, *New J. Phys.* **2015**, *17*, 065018.
[4] B. Yoshimura, M. Stork, D. Dadic, W. C. Campbell, J. K. Freericks, *EPJ Quan. Tech.* **2015**, *2*, 2.
[5] P. Richerme, *Phys. Rev. A* **2016**, *94*, 032320.
[6] S. T. Wang, C. Shen, L. M. Duan, *Sci. Rep.* **2015**, *5*, 8555.
[7] S. Debnath, N. M. Linke, C. Figgatt, K. A. Landsman, K. Wright, C. Monroe, *Nature* **2016**, *536*, 63.
[8] N. Friis, O. Marty, C. Maier, C. Hempel, M. Holzäpfel, P. Jurcevic, M. B. Plenio, M. Huber, C. Roos, R. Blatt, B. Lanyon, *Phys. Rev. X* **2018**, *8*, 021012.

[9] J. Zhang, G. Pagano, P. W. Hess, A. Kyprianidis, P. Becker, H. Kaplan, A. V. Gorshkov, Z. X. Gong, C. Monroe, *Nature* **2017**, *551*, 601.
[10] T. Mitchell, J. Bollinger, D. Dubin, X. P. Huang, W. Itano, R. Baughman, *Science* **1998**, *282*, 1290.
[11] J. W. Britton, B. C. Sawyer, A. C. Keith, C. C. J. Wang, J. K. Freericks, H. Uys, M. J. Biercuk, J. J. Bollinger, *Nature* **2012**, *484*, 489.
[12] J. G. Bohnet, B. C. Sawyer, J. W. Britton, M. L. Wall, A. M. Rey, M. Foss-Feig, J. J. Bollinger, *Science* **2016**, *352*, 1297.
[13] J. I. Cirac, P. Zoller, *Nature* **2000**, *404*, 579.
[14] J. Chiaverini, W. Lybarger Jr, *Phys. Rev. A* **2008**, *77*, 022324.
[15] R. Schmied, J. H. Wesenberg, D. Leibfried, *Phys. Rev. Lett.* **2009**, *102*, 233002.
[16] R. J. Clark, T. Lin, K. R. Brown, I. L. Chuang, *J. Appl. Phys.* **2009**, *105*, 013114.
[17] R. J. Clark, Z. Lin, K. S. Diab, I. L. Chuang, *J. Appl. Phys.* **2011**, *109*, 076103.
[18] M. Kumph, M. Brownnutt, R. Blatt, *New J. Phys.* **2011**, *13*, 073043.
[19] M. Kumph, P. Holz, K. Langer, M. Meraner, M. Niedermayr, M. Brownnutt, R. Blatt, *New J. Phys.* **2016**, *18*, 023047.
[20] R. C. Sterling, H. Rattanasonti, S. Weidt, K. Lake, P. Srinivasan, S. Webster, M. Kraft, W. K. Hensinger, *Nature Commun.* **2014**, *5*, 3637.
[21] M. Mielenz, H. Kalis, M. Wittemer, F. Hakelberg, U. Warring, R. Schmied, M. Blain, P. Maunz, D. L. Moehring, D. Leibfried, T. Schaetz, *Nat. Commun.* **2016**, *7*, 11839.
[22] S. Jain, J. Alonso, M. Grau, J. P. Home, arXiv:1812.06755, **2018**.
[23] M. Block, A. Drakoudis, H. Leuthner, P. Seibert, G. Werth, *J. Phys. B: At. Mol. Opt. Phys.* **2000**, *33*, L375.
[24] K. Okada, M. Wada, T. Takayanagi, S. Ohtani, H. Schuessler, *Phys. Rev. A* **2010**, *81*, 013420.
[25] B. Szymanski, R. Dubessy, B. Dubost, S. Guibal, J. P. Likforman, L. Guidoni, *Appl. Phys. Lett.* **2012**, *100*, 171110.
[26] H. Kaufmann, S. Ulm, G. Jacob, U. Poschinger, H. Landa, A. Retzker, M. Plenio, F. Schmidt-Kaler, *Phys. Rev. Lett.* **2012**, *109*, 263003.
[27] U. Tanaka, K. Suzuki, Y. Ibaraki, S. Urabe, *J. Phys. B* **2014**, *47*, 035301.
[28] L. Yan, W. Wan, L. Chen, F. Zhou, S. Gong, X. Tong, M. Feng, *Sci. Rep.* **2016**, *6*, 21547.
[29] D. Berkeland, J. Miller, J. C. Bergquist, W. M. Itano, D. J. Wineland, *J. Appl. Phys.* **1998**, *83*, 5025.
[30] J. Welzel, A. Bautista-Salvador, C. Abarbanel, V. Wineman-Fisher, C. Wunderlich, R. Folman, F. Schmidt-Kaler, *Eur. Phys. J. D* **2011**, *65*, 285.
[31] A. C. Wilson, Y. Colombe, K. R. Brown, E. Knill, D. Leibfried, D. J. Wineland, *Nature* **2014**, *512*, 57.
[32] F. Hakelberg, P. Kiefer, M. Wittemer, U. Warring, T. Schaetz, *Phys. Rev. Lett.* **2019**, *123*, 100504.
[33] M. Brownnutt, G. Wilpers, P. Gill, R. Thompson, A. Sinclair, *New J. Phys.* **2006**, *8*, 232.
[34] F. Shaikh, A. Ozakin, J. M. Amini, H. Hayden, C. S. Pai, C. Volin, D. R. Denison, D. Faircloth, A. W. Harter, R. E. Slusher, arXiv:1105.4909, **2011**.
[35] G. Wilpers, P. See, P. Gill, A. G. Sinclair, *Nature Nanotech.* **2012**, *7*, 572.
[36] W. Hensinger, S. Olmschenk, D. Stick, D. Hucul, M. Yeo, M. Acton, L. Deslauriers, C. Monroe, J. Rabchuk, *Appl. Phys. Lett.* **2006**, *88*, 034101.
[37] M. J. Madsen, *Ph.D. Thesis*, University of Michigan, **2006**.
[38] S. Olmschenk, K. C. Younge, D. L. Moehring, D. N. Matsukevich, P. Maunz, C. Monroe, *Phys. Rev. A* **2007**, *76*, 052314.
[39] D. Leibfried, R. Blatt, C. Monroe, D. Wineland, *Rev. Mod. Phys.* **2003**, *75*, 281.
[40] D. H. Dubin, *Phys. Rev. Lett.* **1993**, *71*, 2753.
[41] D. Podolsky, E. Shimshoni, G. Morigi, S. Fishman, *Phys. Rev. X* **2016**, *6*, 031025.
[42] J. P. Schiffer, *Phys. Rev. Lett.* **1993**, *70*, 818.
[43] S. Fishman, G. De Chiara, T. Calarco, G. Morigi, *Phys. Rev. B* **2008**, *77*, 064111.
[44] M. Mielenz, J. Brox, S. Kahra, G. Leschhorn, M. Albert, T. Schaetz, H. Landa, B. Reznik, *Phys. Rev. Lett.* **2013**, *110*, 133004.
[45] H. L. Partner, R. Nigmatullin, T. Burgermeister, K. Pyka, J. Keller, A. Retzker, M. B. Plenio, T. E. Mehlstäubler, *New J. Phys.* **2013**, *15*, 103013.
[46] S. Ulm, J. Roßnagel, G. Jacob, C. Degünther, S. Dawkins, U. Poschinger, R. Nigmatullin, A. Retzker, M. Plenio, F. Schmidt-Kaler, K. Singer, *Nature Commun.* **2013**, *4*, 1.
[47] M. Qiao, Y. Wang, Z. Cai, B. Du, P. Wang, C. Luan, W. Chen, H. R. Noh, K. Kim, arXiv:2003.10276, **2020**.
[48] D. Leibfried, *Phys. Rev. A* **1999**, *60*, R3335.
[49] S. L. Zhu, C. Monroe, L. M. Duan, *Phys. Rev. Lett.* **2006**, *97*, 050505.
[50] G. Morigi, Kinks and defects in ion crystals, https://www.youtube.com/watch?v=JvOkdS1zGPY&t=44s (accessed: August 2020).
[51] S. Crain, E. Mount, S. Baek, J. Kim, *Appl. Phys. Lett.* **2014**, *105*, 181115.
[52] D. McGloin, G. C. Spalding, H. Melville, W. Sibbett, K. Dholakia, *Opt. Exp.* **2003**, *11*, 158.
[53] A. Myerson, D. Szwer, S. Webster, D. Allcock, M. Curtis, G. Imreh, J. Sherman, D. Stacey, A. Steane, D. Lucas, *Phys. Rev. Lett.* **2008**, *100*, 200502.
[54] H. Bombin, M. A. Martin-Delgado, *Phys. Rev. Lett.* **2006**, *97*, 180501.
[55] P. Aliferis, A. W. Cross, *Phys. Rev. Lett.* **2007**, *98*, 220502.
[56] R. Raussendorf, J. Harrington, K. Goyal, *New J. Phys.* **2007**, *9*, 199.
[57] H. Bombin, arXiv:1810.09571, **2018**.
[58] M. Newman, L. A. de Castro, K. R. Brown, arXiv:1909.11817, **2019**.
[59] M. Li, D. Miller, M. Newman, Y. Wu, K. R. Brown, *Phys. Rev. X* **2019**, *9*, 021041.
[60] A. Bermudez, X. Xu, R. Nigmatullin, J. O'Gorman, V. Negnevitsky, P. Schindler, T. Monz, U. Poschinger, C. Hempel, J. Home, F. Schmidt-Kaler, M. Biercuk, R. Blatt, S. Benjamin, M. Müller, *Phys. Rev. X* **2017**, *7*, 041061.
[61] M. Müller, A. Rivas, E. Martinez, D. Nigg, P. Schindler, T. Monz, R. Blatt, M. Martin-Delgado, *Phys. Rev. X* **2016**, *6*, 031030.
[62] H. Landa, M. Drewsen, B. Reznik, A. Retzker, *J. Phys. A: Math.Theor.* **2012**, *45*, 455305.
[63] H. Landa, M. Drewsen, B. Reznik, A. Retzker, *New J. Phys.* **2012**, *14*, 093023.